CHF and near-wall boiling behaviors in pool boiling of water on a heating surface coated with nanoparticles

Hiroto Sakashita*

*Division of Energy and Environmental Systems, Graduate School of Engineering, Hokkaido University, North 13 West 8, Kita-ku, Sapporo 060-8628, Japan

* Corresponding author. Tel.: +81 11 706 6664, Fax.: +81 11 706 6664

E-mail address: saka@eng.hokudai.ac.jp

Abstract

This study investigated the saturated pool boiling of water on a 12 mm diameter horizontal heating surface coated with titanium oxide (TiO_2) nanoparticles under atmospheric pressure. The TiO_2 coated surface was formed during nucleate boiling of TiO_2 (25 nm diameter)-water-surfactant nanofluid on the plain heating surface at high heat flux conditions. It was found that the CHF of water boiling on the TiO_2 coated surface increased up to about 1.8 times the CHF for the uncoated (plain) surface. To examine the mechanism of the CHF enhancement by TiO_2 nanoparticle coating, liquid-vapor behaviors close to the heating surface were measured using a conductance probe with a tip diameter smaller than 5 μm. The probe signals and the void fraction distributions showed that there is little difference in the liquid-vapor structure in the boiling on the uncoated surface and on the TiO_2 coated surface, that a liquid rich layer (a so called macrolayer) remains on the heating surface, and that in boiling on the TiO_2 coated surface it does not dry out even at heat fluxes far higher than the CHF of the uncoated surface. The thickness of the macrolayer formed beneath large vapor masses was determined from the location where the probe signals corresponding to the large vapor masses disappear. It was found that the macrolayers formed on the TiO_2 coated surface are thicker than those on the uncoated surface, and it is considered that this is the most likely to be a cause of the CHF enhancement with the TiO_2 coated heating surface.

Key Words: Nanofluids, Critical heat flux, Pool boiling, Conductance probe, Macrolayer thickness

1. Introduction

The boiling of nanofluids (suspensions of nanoparticles dispersed in a base-liquid) has become a topic of increasing interest in energy related engineering fields. A unique characteristic in nanofluid boiling is that the critical heat flux (CHF) is significantly enhanced compared with the CHF of the base-liquid, and on account of this characteristic nanofluids have potential applications as coolants of thermal devices with high heat flux components.

The enhancement of the CHF with nanofluids was reported first by You et al. [1]. They carried out experiments with pool boiling on an upward facing surface with Al_2O_3-water nanofluids at 0.02 MPa and found that the CHF was 3.1 times higher than the CHF of pure water. Vassallo et al. [2] and Milanova and Kumar [3] measured the CHF of SiO_2-water nanofluids on horizontal wires under atmospheric pressure and obtained a 2.0 times increase in the CHF relative to the water. Further, pool boiling experiments with water based nanofluids by Bang and Chang [4] with Al_2O_3 for 4 mm×100 mm surfaces, Kim et al. [5] with Al_2O_3 and TiO_2 for horizontal wires, and Liu et al. [6] with CuO for a 40×40mm surface with microgrooves reported CHF enhancements to be up to 1.5-3.0 times the CHF of water. In addition to these studies of pool boiling, Kim et al. [7] carried out experiments of convective boiling with 55 mm inner diameter vertical tubes. They used Al_2O_3-water, ZnO-water, and diamond-water nanofluids and obtained 1.4 to 1.5 times enhancements of the CHF at mass flow rates of 2000-2500 kg/m^{2}s. Ahn et al. [8] measured the CHF for forced convective boiling of Al_2O_3-water nanofluids on a 10mm diameter upward facing disk, and reported 1.4 times the CHF of water.

It has been recognized that nanoparticles are deposited on heating surfaces during boiling of nanofluids and the wettability of the deposited surfaces

is significantly improved (the static contact angle decreases significantly). Kim and Kim [9] boiled different nanofluids on 0.2 mm diameter horizontal wires to provide deposition layers of the nanoparticles on the wires, and reported that the static contact angle of the nanoparticle coated wires decreases and the CHF of water on the nanoparticle coated wires increases with decreasing contact angle. Kwark et al. [10] measured the CHF of water boiling on a 10 mm×10 mm surface on which a Al_2O_3 nanoparticle coated layer was previously deposited by nucleate boiling of a Al_2O_3-water/ethanol nanofluid. Here it was found that the CHF increases linearly with the decrease in the contact angle.

As mentioned above, valuable information on CHF enhancement with nanofluids has been reported, however, the mechanism of the CHF enhancement has not been fully elucidated. To investigate the mechanism of CHF enhancement with nanofluids, the present study carried out experiments with pool boiling of water on a 12 mm diameter upward facing surface coated with TiO_2 nanoparticles. The liquid-vapor structures near the TiO_2 coated surface were closely examined based on measurements with a conductance probe. Through these measurements, the thicknesses of the liquid layer (macrolyer) formed beneath vapor masses were established, and the reason why the TiO_2 coated surface can enhance the CHF of water is discussed.

2. Experiment

2.1 Experimental apparatus

The experiments were carried out in saturated pool boiling of water under atmospheric pressure. Fig.1 shows the experimental apparatus. The heating surface is the upper end of a 12 mm diameter cylindrical copper block. A 1 mm thick stainless steel flange was silver-soldered around the copper heating surface.

The surfaces of the copper and the surrounding flange were machined to be flush, and then Ni was plated over the two surfaces to avoid corrosion and nucleation of bubbles at the interface between the copper surface and the flange. The surface heat flux and the surface superheat were determined with two 0.5 mm diameter thermocouples, which were embedded in the copper block 4 and 12 mm below the horizontal top surface. The boiling vessel is made of Pyrex glass with an inner diameter of 150 mm. The two auxiliary heaters were installed in the boiling vessel and those were used for heating and degassing the water. Prior to each measurement, 1.6L of de-ionized water with electro-conductivity below 0.2μS/cm was poured into the vessel, then boiled for 30min to remove dissolved gasses. The water temperature during the measurements was monitored with a sheathed thermocouple inserted in the thermocouple well.

The liquid-vapor behaviors close to the heating surface were measured with a conductance probe. The tip of the conductance probe was thinned to less than 5 μm by electro-polishing. The conductance probe was connected to a three-dimensional moving stage with an accuracy of 0.5 μm in the vertical and 10 μm in the horizontal direction. During the measurements, KCl (potassium chloride) was added to increase the electro conductivity of the water, and an A.C. voltage was imposed between the heating surface and the probe. The concentration of the KCl was less than 100 ppm and changes in the surface tension as well as other thermo-physical properties of the water by adding the KCl were negligibly small.

The measurement arrangements with the conductance probe are described in detail in reference [11] by Ono and Sakashita. An A.C. voltage of 24 kHz, the resonance frequency of the measurement circuit, was applied between the conductance probe and the heating surface, and the inverse of the resonance

frequency of the electrical circuit, 42 μs, was the time resolution of the measurements. The raw 24 kHz signals from the probe were digitized with an adequate threshold voltage by comparator circuits and converted into continuous signals by a RE TRIG.S/S (re-triggerable single shot) circuit.

The probe position normal to the heating surface was calibrated by the electrical contact between the probe tip and the heating surface by using a short detection circuit which can establish the point when the peak voltage and/or the frequency of the probe signals become lower than a given threshold value. The contact between the probe tip and the heating surface could be detected for the TiO_2 coated surface as well as for the uncoated surface. For the TiO_2 coated surface, it was thought that the probe tip penetrated through the TiO_2 layer and that the short detection circuit detected the contact of the probe tip with the Ni plated copper surface underneath the TiO_2 layer. Therefore, the actual probe position for the TiO_2 coated surface and the position determined by the electric contact may differ by the coated layer thickness. As mentioned in Section 3.1, however, the TiO_2 layer thickness was estimated to be thinner than 1 μm, and the error of the probe position for the TiO_2 coated surface is also smaller than 1 μm, the same order of magnitude as the accuracy of the moving stage, 0.5 μm.

Examples of raw signals from the probe and the converted digitized signals are shown in Fig.2, where a high voltage of the raw signal shows that the tip of the probe is in contact with vapor and a low voltage that it is in contact with liquid. In this paper, a digitized binary signal with high-level is termed a pulse and its width is the pulse width.

2.2 Preparation of TiO_2 coated heating surface

The experiments used TiO_2 nanoparticles (Sigma-Aldrich) with a

vendor-specified average size of nanoparticles of 25 nm. Fig.3 shows a SEM image of the nanoparticles in a dry state. The size distribution and the state of agglomeration of the nanoparticles in the suspension were not measured in the present experiment. The TiO_2 coated surface was prepared by nucleate boiling of TiO_2-water nanofluid in the following manner: 0.018 g of TiO_2 nanoparticles were mixed with 0.1 L of de-ionized water, and dispersed in an ultrasonic bath for 30 min. Further, 1.6 L of de-ionized water was poured into the boiling vessel shown in Fig.1, and 0.17 g of surfactant (SDS, Sodium Dodecylsulphate) was added to the water, aiming to promote uniformity of the coated layer since addition of surfactant into the water drastically decreases the size of primary bubbles and increases the number of nucleation sites. This SDS aqueous solution was brought to boil and the heat flux of the heated copper block was adjusted to 1MW/m^2. After boiling was continued for 30 min for degassing, the TiO_2-water suspension (0.1 L) was poured into the boiling vessel, and the nucleate boiling at 1MW/m^2 was continued for 8min, before the heating of the copper block was discontinued. The initial concentration of TiO_2 nanoparticles in the boiling vessel was 0.0011 wt% and the SDS concentration 0.010 wt%.

The TiO_2 coated layer developed by the above procedure adhered quite firmly on the Ni plated copper surface, but a part of the coated layer was at times dislodged during repeated measurements at high heat fluxes close to the CHF. Therefore, the experiments were carried out with a coated surface that was newly prepared using the above procedure before each run. Reproducibility of the TiO_2 coating condition was evaluated by observations of the appearance of the TiO_2 coating, estimation of the maximum thickness of the coated layer, and measurement of the static contact angle. As described in detail in the following section 3.1, the reproducibility of the TiO_2 coating appeared to be satisfactory.

3. Results and discussion

3.1 Appearance of nano-coating and thickness of the nano-coated layer

Figs.4-(a) and 4-(b) show the appearance of the TiO_2 coated heating surface. In Fig.4-(a), showing the whole surface (12 mm diameter heating surface encircled with a broken line), some areas near the periphery of the heating surface remain uncoated, but the central part of the surface appears to be coated uniformly. Fig.4-(b) is an enlargement of the 1 mm square enclosed area from the central part of the surface, showing that a uniform coated layer is covering the surface. The appearances of all the TiO_2 coatings on newly coated surfaces were observed, and while the coatings near the periphery varied somewhat, most of the surface was covered with a uniform TiO_2 layer, similarly to that in Fig.4. Measurements of the liquid-vapor behaviors with the conductance probe detailed in the following sections were carried out at the center of the heating surface.

The thickness of the TiO_2 coated layer was estimated in the following manner: the probe was placed above an uncoated area and a zero-position of probe height was specified by contacting the probe tip with the surface. Then, the probe was raised slightly, and moved horizontally to over a TiO_2 coated area while observing the probe tip with a microscope. For all TiO_2 coated surfaces used in the present experiments, the probe moved smoothly from the uncoated area to the coated area without scratching the surface of the coated layer when the probe tip was 1 μm or further from the surface of the uncoated area. Therefore, it was determined that the maximum thickness of the TiO_2 coated layer was smaller than 1μm, and that the reproducibility of the coated layer thicknesses on the surface was within 1μm.

Fig.5 shows water droplets (3 μL) placed on the uncoated surface

(Fig.5-(a)) and on a TiO_2 coated surface (Fig.5-(b)). As in previous studies, the 75 degree static contact angle θ of the uncoated surface is much smaller, 5deg., with the TiO_2 coated surface, indicating an improvement in wettability due to the deposition of the TiO_2 nanoparticles. The static contact angle of the TiO_2 coated surface was measured before each run, and all showed very similar values, around 5deg.

3.2 Boiling curves and critical heat fluxes

The boiling curves were obtained by gradually increasing the heat input to the cartridge heaters installed in the copper block until the CHF condition was reached. The outputs from the thermocouples were recorded at 0.5 s time intervals, and the heat input was controlled manually so the rate of increase in the surface temperature did not exceed 1.0K/min in the nucleate boiling region. When the rapid increase in surface temperature was detected, then the data acquisition was terminated and the heat input was discontinued. The CHF was defined as the highest heat flux on the boiling curve calculated using the acquired temperature data.

Fig.6 shows the boiling curves measured with the uncoated and the TiO_2 coated surfaces. Similar to previous studies, the CHF of the coated surface is enhanced 1.7-1.8 times compared with that of the uncoated surface. The nucleate boiling curves for both surfaces lie close to the results predicted with the correlation for water by Stephan and Abdelsalam [12], but the boiling curves of the TiO_2 coated surface shift toward a slightly lower superheat, showing the heat transfer enhancement by the TiO_2 deposition. The slight difference between two boiling curves (run 1 and run2) for the TiO_2 coated surface may be due to the differences in the TiO_2 coating condition near the periphery of the heating surface.

3.3 Boiling behaviors at high heat fluxes and definition of vapor mass signals

3.3.1 Pulse width spectrum

At high heat fluxes in nucleate pool boiling on an upward facing heating surface, large coalesced bubbles are formed, and a liquid rich layer rests beneath the coalesced bubbles. Previous research has commonly termed the large coalesced bubble, “vapor mass”, and the liquid rich layer, “macrolayer”.

Fig.7 shows the pulse width spectrums of 8192 sequential pulses measured at 1.64MW/m^2 for the TiO_2 coated surface at two distances (h=0.05 and 2.0 mm) from the heating surface. The vertical axis of Fig.7 expresses the number of pulses counted within the time of the measurements. In Fig.7, the spectrum obtained at h=2.0 mm has a peak in the region of pulse widths from about 20ms to 55ms, and this peak disappears near the heating surface as shown by the spectrum at h=0.05 mm. Therefore, the peak may be assumed to be caused by pulses corresponding to so called “vapor masses”. However, it seems insufficient to identify vapor mass signals based only on the pulse width spectrums. This paper determines the macrolayer thicknesses from the location of disappearance of the vapor mass signals as will be described in Section 3.6, and a more rigorous specification of the pulses corresponding to the vapor masses is necessary. For this, simultaneous measurements of the boiling behaviors using high speed video and the conductance probe were carried out at high heat flux conditions with both uncoated and TiO_2 coated surfaces, as will be detailed in the following section.

3.3.2 Behavior of coalesced bubbles and definition of vapor mass signals

To detect the signals of the vapor masses, the probe was placed 2 mm above the heating surface at the center of the heating surface, and at the same

time, the boiling behavior was recorded with high-speed video at frame rates of 500 to 1000 fps. Figs.8-(a) to 8-(d) show photos of the video images, with typical examples of the coalesced bubbles observed in the present experiment. The horizontal broken lines drawn in the figures show the level of the tip of the conductance probe (2mm above the heating surface). As with the previous studies of pool boiling of water on relatively small surfaces at high heat fluxes, two types of coalesced bubbles were observed in the present experiment: Mushroom-like large bubbles that grow with little interference from preceding detached coalesced bubbles to reach a size larger than the diameter of heating surface (Figs.8-(a) and (b)), and column-like coalesced bubbles that are formed immediately after the detachment of a preceding coalesced bubble, and then quickly absorbed into the preceding bubble and not developing into a large mushroom-like bubble (Figs.8-(c) and (d))

To specify the correspondence between the size of the coalesced bubbles and the probe signals, the width of the coalesced bubble, D_w, at the height of the probe tip (h=2mm) was measured from the video records, and compared with the probe signals. Fig.9 shows the variations of D_w with time, together with the simultaneously obtained binary probe signals measured for the TiO_2 coated surface at 1.96MW/m^2. The measurements were carried out over 5 s, but only the data for the first 0.5 s after the start of the measurements are presented in the figure. Here, the images in Figs.8-(a) to (d) correspond to the boiling appearances at the moments indicated by arrows (a) to (d) in Fig.9. There is good correlation between the magnitudes of D_w and the widths of the corresponding pulses: D_w corresponding to wider pulses show larger values.

As the next step to identify the vapor mass signals, the local maximum of D_w, (described as $D_{w,max}$) within each pulse was specified from the data of D_w, and

plots against the width of corresponding pulses in Fig.10, where the data for both the uncoated surface (q=1.25MW/m^2) and the TiO_2 coated surface (q=1.63 and 1.96MW/m^2) are shown. In Fig.10, the symbols in blue show the mushroom-like bubbles and the symbols in black show the column-like bubbles. The figure shows that the regions of the two types of coalesced bubbles at three different heat fluxes are separated by similar pulse widths of 20 ms: pulses wider than 20 ms corresponding to the mushroom-like bubbles and pulses narrower than 20 ms corresponding to the column-like bubbles. When it is assumed that the CHF is caused by the dryout of the macrolayer beneath the coalesced bubbles, it may be hypothesized that the coalesced bubbles responsible for the occurrence of the CHF are not the column-like bubbles but the mushroom-like bubbles corresponding to the wider pulses (longer hovering periods). This paper, therefore, assumes that pulse with widths of 20 ms or wider corresponds to the vapor masses, and the region of pulse widths wider than 20 ms is termed the “vapor mass region”.

3.4 Vertical distributions of void fractions and pulse frequencies

As shown in the preceding section, in the present experiments with a 12 mm diameter heating surface, large coalesced bubbles (vapor masses) completely covering the heating surface were formed at high heat fluxes for both the uncoated and coated surfaces. The results shown in the following were obtained under the high heat fluxes where the vapor masses are formed. Moving the probe in the vertical direction, a total 4096 or 8192 pulses were acquired at every elevation above the heating surface. The time averaged void fractions and the pulse frequencies (frequencies of the probe tip- vapor contact) shown in Figs.11-13 are values obtained by the total pulse widths and the total pulse number divided by the length of time of measurements. Figs.11 shows the vertical distributions of

the time averaged void fractions for the uncoated surface and Fig.12 is for the TiO_2 coated surface all measured at the center of the heating surface. There are no marked differences between the void fraction profiles of the uncoated and the coated surfaces; the void fraction increases when approaching the heating surface, reaches a maximum, and then decreases steeply. Further, the void fractions for all heat fluxes reach zero or a constant value very close to zero near the surface, indicating that there is a liquid layer (the so called macrolayer) between the heating surface and the vapor mass. The highest heat flux in Fig.12 for the coated surface (2.0 MW/m^2) is much higher than the CHF of the uncoated surface (1.3 MW/m^2). Even at this high heat flux, the void fraction is zero close to the heating surface, showing that the macrolayer does not dry out but remains on the TiO_2 coated surface at the departure of vapor masses.

Fig.13 shows the distributions of pulse frequencies for the uncoated and the TiO_2 coated surfaces. The distributions are very similar, initially there is an increase to reach a maximum at a 0.1-0.2mm height, and then a rapid decrease with increasing distance from the heating surface. The increase in the frequency is caused by an increase in the number of discontinuities in the vapor mass signals, as shown in the probe signals at h=0.2mm in Fig.3. This may, therefore, be interpreted to show that the high frequency of the pulse signals would be caused by intermittent contact of the probe tip with liquid/vapor due to intensive oscillation of the bottom of the vapor mass.

3.5 Hovering periods of vapor masses

As shown in Fig.7, the vapor mass signals are distributed over a range of pulse widths (as mentioned in section 3.3, and the pulses wider than 20ms are defined as the vapor masses). Therefore, an averaged value (a weighted

arithmetic mean) of the pulse widths corresponding to the vapor mass region was calculated from the pulse width spectrum, and was defined as the hovering period for a given heat flux. Fig.14 shows the hovering periods versus the heat fluxes, where the symbols are the averaged values and the vertical bars show the minimum (20 ms) and maximum hovering periods. The average hovering periods increase moderately with the increase in the heat flux, and there are no marked differences for the uncoated and the TiO_2 coated surfaces. Especially at heat fluxes near the CHF of the uncoated surface, the hovering periods are very similar for the uncoated and the TiO_2 coated surfaces. Therefore, the improvement in surface wettability due to TiO_2 deposition has no apparent effect on the vapor mass behaviors and the enhancement of the CHF for the TiO_2 coated surface is not explained by the differences in the vapor mass hovering periods.

3.6 Macrolayer thickness formed beneath vapor masses

Ono and Sakashita [11] have reported liquid-vapor behaviors near a horizontal heating surface using conductance probes in saturated and subcooled pool boiling of water under atmospheric pressure. They assumed that the region from the heating surface to the height below which the oscillation of the interface at the bottom of the vapor mass does not reach corresponds to the so called macrolayer, from this it was possible to specify the thickness of the macrolayer from the location where the vapor mass signals disappear. Here, the author determined the macrolayer thickness based on the same assumptions.

Full details of the method to determine the macrolayer thickness are represented in the previous paper (Ono and Sakashita [11]), and only an outline of the method is given next.

The time-series data of the pulse signals were measured at various heights

over the heating surface (total number of pulses 4096 or 8192). Then, the pulses obtained at each height were classified into groups for every 2 ms of pulse width, and the frequency of the appearance of pulses of each pulse group was plotted. An example for the TiO_2 coated surface and heat flux of 1.47 MW/m^2 is shown in Fig.15 with the frequencies of appearance for the 2-4 ms, 14-16 ms, 30-32ms, and 44-46ms pulse groups plotted against the height over the heating surface. In Fig.15, the 14-16ms pulse group disappears at a height of about 0.04mm and the 44-46ms group at about 0.12mm. In this manner, the height at which the frequency of appearance reaches zero was determined for each pulse group and is plotted in the top graph of Fig.16. Here, the height of disappearance of the pulse groups with very wide pulse widths are not included because the number of pulses in these groups are too few to show a smooth distribution of the frequencies of appearance. The bottom graph of Fig.16 is the spectrum of pulse widths obtained 2.0 mm over the heating surface. From the spectrum of the pulse widths, the pulses corresponding to the vapor masses can be specified (in the bottom graph in Fig.16, pulses from 20 ms to 49 ms were specified to correspond to the vapor masses), and the locations of the disappearance within the vapor mass region were regarded as the macrolayer thicknesses. As shown in the top graph of Fig.16, the macrolayer thicknesses distribute over a wide range, and vapor masses with narrower pulse widths (with shorter hovering periods) have thinner macrolayers at their bottom. Further, comparing the top and bottom graphs, the macrolayers with different thicknesses have different formation frequencies: the macrolayer corresponding to the peak of the spectrum (pulse width 36 ms) has the highest formation frequency, and the macrolayers corresponding to narrower and wider pulse widths than the peak value have relatively low formation frequencies. This paper therefore, assumes that the averaged value of the macrolayer thicknesses,

$\delta_{m,ave}$, weighted by the formation frequency was calculated with equation (1), and this averaged value is considered the macrolayer thickness for a specified heat flux condition.

$$\delta_{m,ave} = \sum_{i=1}^{n} \delta_{m,i} \cdot f_i \Big/ \sum_{i=1}^{n} f_i \qquad (1).$$

Here i is number of pulse groups in the vapor mass region (i=1 means 20-22 ms pulse group, and $i = n$ is a pulse group with the widest pulse width), f_i and $\delta_{m,i}$ are the pulse number and the thickness of the macrolayer of *i-th* pulse group, respectively.

Here it must be pointed out that the previous paper by Ono and Sakashita [11] determined the macrolayer thickness from the averaged value of several data points at the position of disappearance around the peak of the spectrum, rather than using equation (1) (In the case of Fig.16, the averaged value around the pulse width of 36 ms was regarded as the macrolayer thickness). From a purely practical standpoint, there is little differences in the macrolayer thicknesses determined by the previous and the present methods, because, in most cases, the averaged values calculated using equation (1) lie close to the values around the peak of the spectrum, as with the case of Fig.16. However, it seems that the definition of the macrolayer thickness according to the method presented in this paper is superior, because the variations in the thickness and formation frequencies of the macrolayer within the vapor mass region are considered. This is the reason why this paper has modified the previous method into the method based on equation (1).

The macrolayer thicknesses determined according to the above procedures are shown in Fig.17. In Fig.17, the symbols are for the averaged values calculated using equation (1) and the vertical bars at each symbol indicate the minimum and

maximum values. The macrolayer thicknesses predicted with the empirical correlations proposed by Bhat et al. [13] and Rajvanshi et al. [14] for pool boiling of water on horizontal surfaces, and with the semi-theoretical correlation by Haramura and Katto [15] are also shown in Fig.17. The data for the uncoated surface lie between the predicted results with the Haramura and Katto correlation and the correlations by Bhat et al. or Rajvanshi et al. However, the data for the TiO_2 coated surface show thicker layers than the data for the uncoated surface as well as thicker than the extrapolations of the various correlations to higher heat flux regions.

3.7 Transient behavior of void fraction near heating surface before and after the CHF

As shown in the previous section, the TiO_2 coated surface is covered by a macrolayer that is not subject to dryout even at heat fluxes far higher than the CHF of the surface not coated by TiO_2, and that the macrolayer formed on the TiO_2 coated surface is thicker than that on the uncoated heating surface. Therefore, there is a possibility that the thicker macrolayer is responsible for the enhancement of the CHF of the TiO_2 coated surface, if the CHF is triggered by dryout of the macrolayer as assumed by the macrolayer dryout model. To further investigate the possibility of a trigger mechanism of the CHF, the transient behaviors of the void fractions close to the heating surface before and after CHF were measured under transient heating modes. The probe was placed 15 μm over the surface, and the probe signals and the outputs of the two thermocouples embedded in the copper block (4 and 12 mm below the top surface) were recorded simultaneously from the nucleate boiling region through the CHF to the

transition boiling region under the transient heating mode, realized by stepwise increases in heat input to the copper block initially kept at steady-state conditions at high heat fluxes with nucleate boiling. The sampling rate of the thermocouple outputs and the probe signals were 0.5 s and 50 μs, respectively. Figs.18-(a) (uncoated surface) and 18-(b) (TiO_2 coated surface) show the void fractions obtained by averaging the probe signals for every 0.5 s period together with the corresponding surface heat fluxes.

The surface heat fluxes in Fig.18 are the values calculated from the readings of the two thermocouples embedded in the copper block. The time delay in the response of the thermocouple at the position nearest to the heating surface (4 mm below the surface) to the change in surface temperature is estimated to be 13-40 ms. Therefore, the thermocouple responses may include a time delay during which one or two vapor masses detach, but no correction for this was made in calculating the surface heat flux.

In Fig.18-(a) for the uncoated surface, the heat flux commences to decrease at 129 s after the measurements started, then after a slight increase it decreases sharply again from 137 s, showing that the CHF has been reached. The void fraction averaged for every 0.5 s is recorded as close to zero until 129 s, then it begins to increase, however with large fluctuations, from 129 s and it increases steeply at around the time of the CHF. The results with the TiO_2 coated surface in Fig.18-(b) are similar to the case with the uncoated surface: the void fraction remains at small values close to zero until 80 s after the start of measurements. (The heat fluxes in this period are far higher than the CHF of the uncoated surface.) When the heat flux begins to fluctuate after 80s, the void fractions also show large fluctuations, and abruptly rise at almost the same time as the occurrence of CHF at around 100 s. Fig.19 shows digitized probe signals around

the time of the CHF for the TiO_2 coated surface. At the time of the CHF, the probe signals change from narrow signals with low frequency (corresponding to fluctuations of the base of the vapor masses) to high and frequent wide signals showing that the surface is in the dryout condition during most of the vapor mass hovering periods.

The results shown in Figs. 17 to 19 strongly suggest that for both the uncoated and TiO_2 coated surfaces, the surface is covered with a macrolayer before the CHF and that the dryout of this macrolayer triggers the occurrence of the CHF. Therefore, the trigger mechanism of the CHF appears to be very similar to the macrolayer dryout model and the cause of the CHF enhancement for the TiO_2 coated surface is that a thick macrolayer was able to form as suggested in Fig.17.

The reasons why the thicker macrolayer is formed on the TiO_2 coated surface have not been satisfactorily explained, but Wang and Dhir [16] and Imai et al. [17] have reported that improvements in surface wettability can significantly reduce nucleation site density. Wang and Dhir improved wettability by changing the degree of oxidation of copper surfaces, and Imai et al. by irradiating an oxidized heating surface (0.5mm wire) with gamma rays. (The improvement in wettability by gamma ray irradiation was first established by Takamasa et al. [18], who termed this phenomenon RISA (Radiation Induced Surface Activation)). Although the present study did not measure the nucleation site density, there is a possibility that the nucleation site density is lowered by the TiO_2 coated surface due to the improvement in wettability. When the macrolayer is assumed to be formed by the coalescence of primary bubbles, the macrolayer thickness is approximately proportional to the size of the primary bubbles at coalescence. Reduction in the nucleation site densities results in an increase in

the size of the primary bubbles at coalescence, and hence could thicken the macrolayer. The improvement in surface wettability may, therefore, be one of the causes of the formation of the thicker macrolayer.

4. Conclusions

Liquid-vapor behaviors were measured using a conductance probe during pool boiling of water on an upward-facing heating surface coated with TiO_2 nanoparticles. The conclusions obtained by the present study may be summarized as follows.

(1) The CHF of the TiO_2 coated surface is enhanced 1.7-1.8 times compared with that of the uncoated surface.

(2) There are only small discrepancies in the distributions of time averaged void fractions and pulse frequencies between the uncoated and the TiO_2 coated surfaces. The only difference is that the TiO_2 coated surface was covered with liquid even at heat fluxes higher than the CHF of the uncoated surface.

(3) The thickness of the macrolayer beneath vapor masses was determined from the height over the heating surface where the vapor mass signals disappear. It was found that the macrolayer on the TiO_2 coated surface is thicker than would be expected by an extrapolation of the macrolayer thickness for the uncoated surface to higher heat flux regions.

(4) The simultaneous measurements of the void fractions and heat fluxes under transient heating showed that, for both the uncoated and TiO_2 coated surfaces, the void fraction 15 μm above the heating surface remained at values of around zero in the nucleate boiling region before the CHF, and increased steeply just at the CHF. This suggests that the CHF is triggered by the dryout of the macrolayer for both the uncoated and TiO_2 coated surfaces.

(5) From the conclusions in (2)-(4), the formation of a thicker macrolayer may be a cause the CHF enhancement of the TiO_2 coated surface.

References

[1] You, S. M., Kim, J. H. and Kim, K. H., Effect of nanoparticles on critical heat flux of water in pool boiling heat transfer, *Appl. Phys. Lett.*, 83-16(2003) 3374-3376.

[2] Vassallo, P., Kumar, R. and D'Amico, S., Pool boiling heat transfer experoments in silica-water nano-fluids, *Int. J. Heat Mass Transfer*, 47(2004) 407-411.

[3] Milanova, D. and Kumar, R., Role of ions in pool boiling heat transfer of pure and silica nanofluids, *Appl. Phys. Lett.*, 87, 233107(2005).

[4] Bang, I. C. and Chang, S.H., Boiling heat transfer performance and phenomena of Al_2O_3-water nanofluids from a plain surface in a pool, *Int. J. Heat Mass Transfer*, 48(2005) 2407-2419.

[5] Kim, H. Kim, J. and Kim M. H., Effect of nanoparticles on CHF enhancement in pool boiling of nanofluids, *Int. J. Heat Mass Transfer*, 49(2006) 5070-5074.

[6] Liu, Z. H., Xiong, J. G. and Bao, R., Boiling heat transfer characteristics of nanofluids in a flat heat pipe evaporator with micro-grooved heating surface, *Int. J. Multiphase flow*, 33(2007) 1284-1295.

[7] Kim, S. J., McKrell, T., Buongiorno, J. and Hu, L. W., Experimental study of flow critical heat flux in alumina-water, zinc-oxide-water, and diamond-water nanofluids, 2009, *J. Heat transfer*, 131(2009) 043204.

[8] Ahn, H. S., Kim, H., Jo, H., Kang, S., Chang, W. and Kim, M.H., Experimental study of critical heat flux enhancement during forced convective flow boiling of nanofluid on a short heater surface, *Int. J. Multiphase flow*, 36(2010) 375-384.

[9] Kim, H.D. and Kim, M. H., Effect of nanoparticle deposition on capillary wicking that influences the critical heat flux in nanofluids, *Appl. Phys. Lett.* 91, 014104 (2007).

[10] Kwark, S. M., Moreno, G., Kumar, R., Moon, H. and You, S.M., Nanocoating

characterization in pool boiling heat transfer of pure water, *Int. J. Heat Mass Transfer*, 53(2010) 4579-4587.

[11] Ono, A. and Sakashita, H., Liquid-vapor structure near heating surface at high heat flux in subcooled pool boiling, *Int. J. Heat Mass Transfer*, 50(2007) 3481-3489.

[12] Stephan, K. and Abdelsalam, M., Heat-transfer correlations for natural convection boiling, *Int. J. Heat Mass Transfer*, 20(1980) 73-87.

[13] Bhat,A.M, Prakash,R. and Saini,J.S., On the mechanism of macrolayer formation in nucleate pool boiling at high heat flux, *Int. J. Heat Mass Transfer*, 26-5(1983) 735-739..

[14] Rajivanshi,A.K., Saini, J.S. and Prakash, R., Investigation of macrolayer thickness in nucleate pool boiling*, Int. J. Heat Mass Transfer*, 35-2 (1992) 343-350.

[15] Haramura,Y. and Katto, Y., A new model of critical heat flux, applicable widely to both pool and forced convection boiling on submerged bodies in saturated liquids, *Int. J. Heat Mass Transfer*, 26-3(1983) 389-398.

[16] Wang, C. H. and Dhir, V. K., Effect of surface wettability on active nucleation site density during pool boiling of water on a vertical surface, *J. Heat Transfer*, 115(1993) 659-669.

[17] Imai, Y., Okamoto, K., Madarame, H. and Takamasa, T., Reduction of active nucleation site density under gammma ray irradiation, *Thermal Sci. and Eng.*, 13-5(2005) 17-23.

[18] Takamasa, T., Hazuku, T., Mishima, K., Okamoto, K., and Imai, Y., Surface wettability caused by radiation induced surface activation, *Thermal Sci. and Eng.*, 12-2(2004) 41-46.

CAPTIONS OF FIGURES

Fig.1 Outline of the experimental apparatus.

Fig.2 Examples of probe signals.

Fig.3 SEM image of TiO_2 nanoparticle

Fig.4 Images of a TiO_2 coated surface. (a) The whole surface (the circle shows the 12 mm diameter heating surface) (b) Enlargement of the area of the central part of the heating surface

Fig.5 Static contact angles, θ, of a water droplet on (a) uncoated surface and (b) TiO_2 coated surface. (a) uncoated surface (θ=75 deg.) (b) TiO_2 coated surface (θ=5 deg.)

Fig.6 Boiling curves for uncoated and TiO_2 coated surfaces.

Fig.7 Pulse width spectrums above the heating surface at h=0.05 mm and h=2 mm

Fig.8 Boiling appearance (TiO_2 coated surface, $q=1.96MW/m^2$)

Fig.9 Width of coalesced bubbles and binary probe signals measured at 2mm above the heating surface

Fig.10 Plot of the maximum width of coalesced bubbles and pulse widths

Fig.11 Void fraction distributions (uncoated surface).

Fig.12 Void fraction distributions (TiO_2 coated surface).

Fig.13 Pulse frequency distributions.

Fig.14 Hovering periods of vapor masses for the uncoated and TiO_2 coated surfaces.

Fig.15 Frequency distributions for the 2-4, 14-16, 30-32, and 36-38 ms-wide pulses.

Fig.16 Distance from the heating surface where pulses disappear and the incidence of pulses at h=2 mm.

Fig.17 Macrolayer thickness for the uncoated and TiO_2 coated surfaces

Fig.18 Change in heat fluxes and void fractions at h=15 μm before and after the CHF. (a) Uncoated surface (b) TiO_2 coated surface

Fig.19 Digitized probe signals before (left) and after (right) CHF.

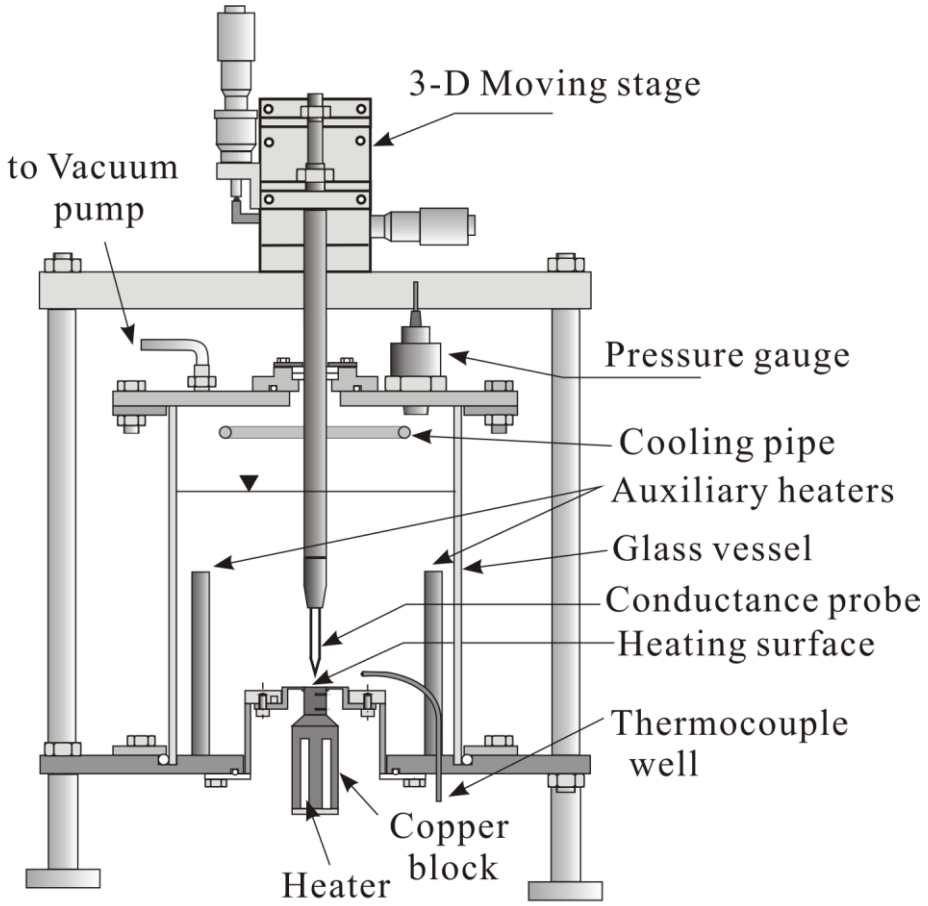

Fig.1 Outline of experimental apparatus

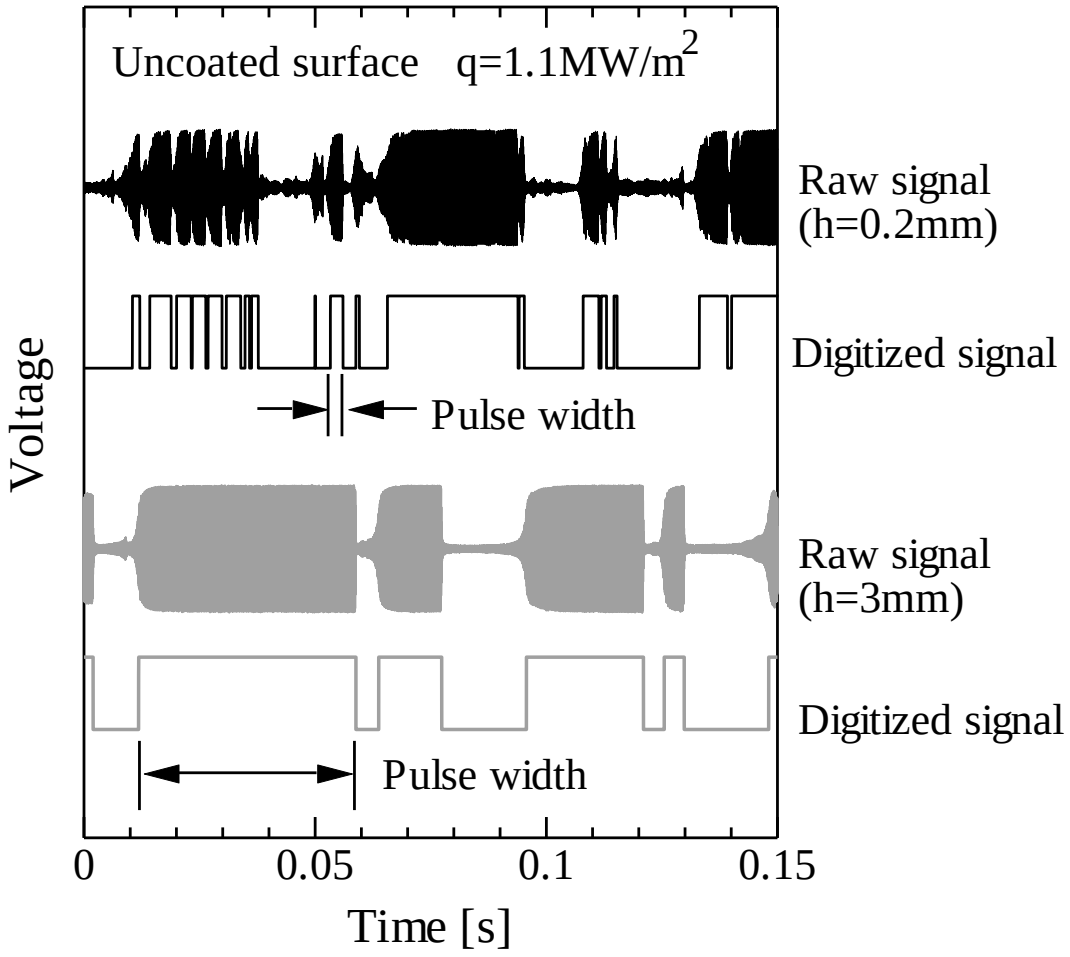

Fig.2 Examples of probe signals

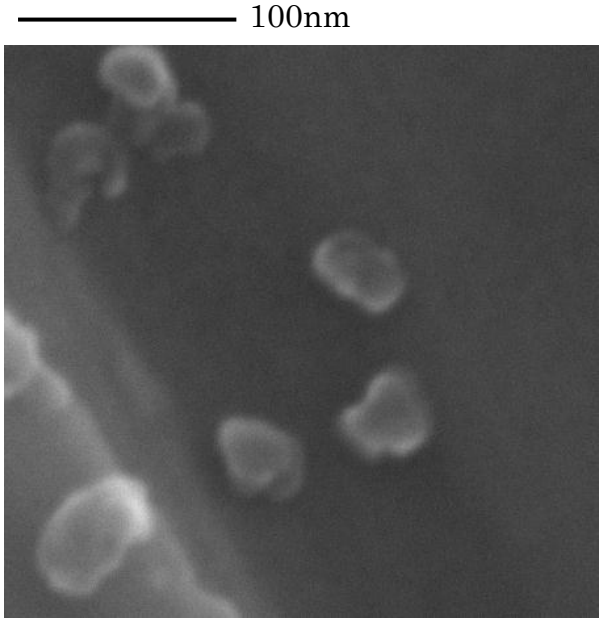

Fig.3 SEM image of TiO_2 nanoparticle

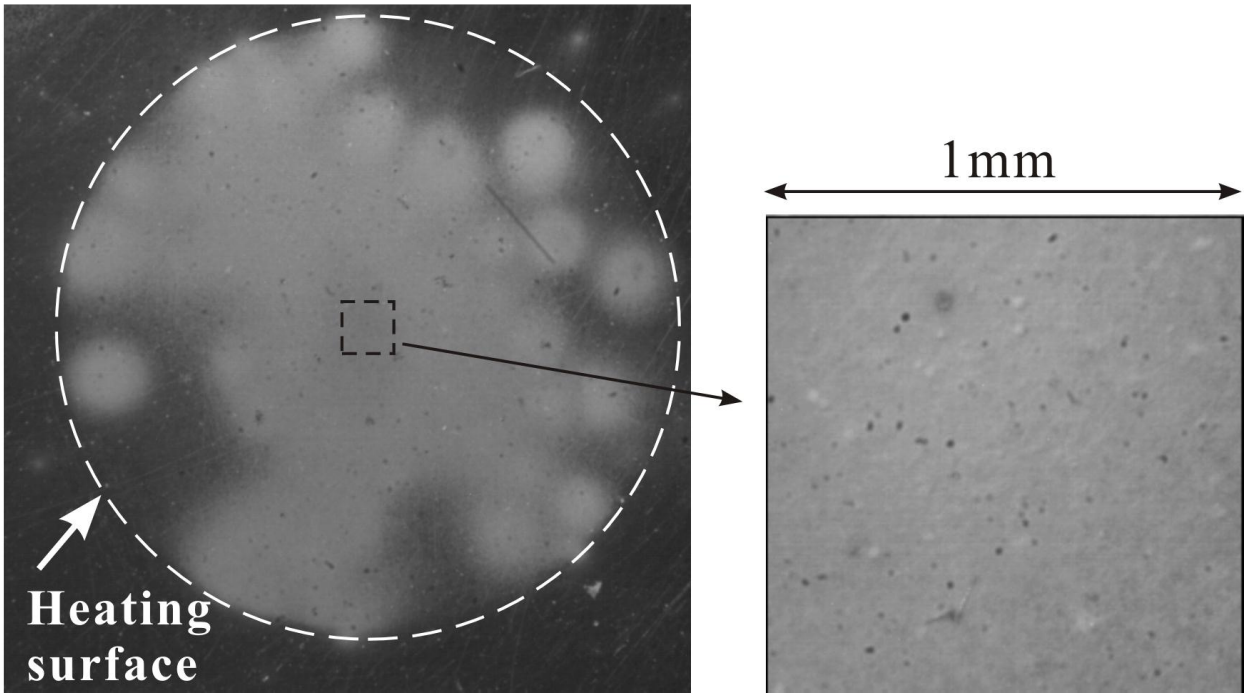

(a) Whole surface (the circle shows the 12 mm diameter heating surface)

(b) Enlargement of the area of the central part of the heating surface

Fig.4 Images of a TiO_2 coated surface

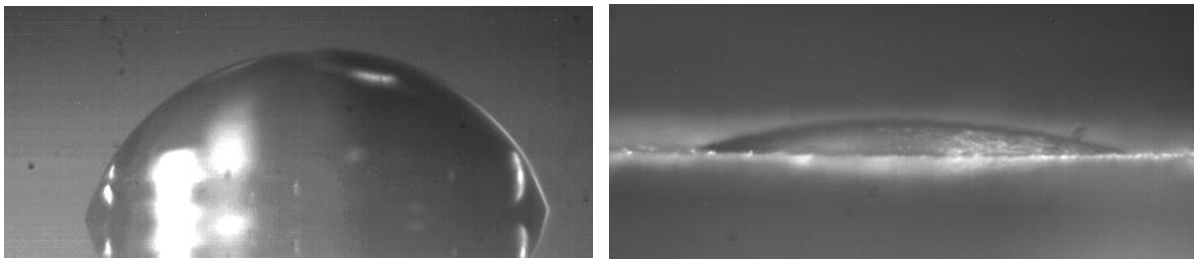

(a) Uncoated surface (θ=75 deg.)　　(b) TiO_2 coated surface (θ=5 deg.)

Fig.5 Static contact angles, θ, of a water droplet on (a) uncoated surface and (b) TiO_2 coated surface

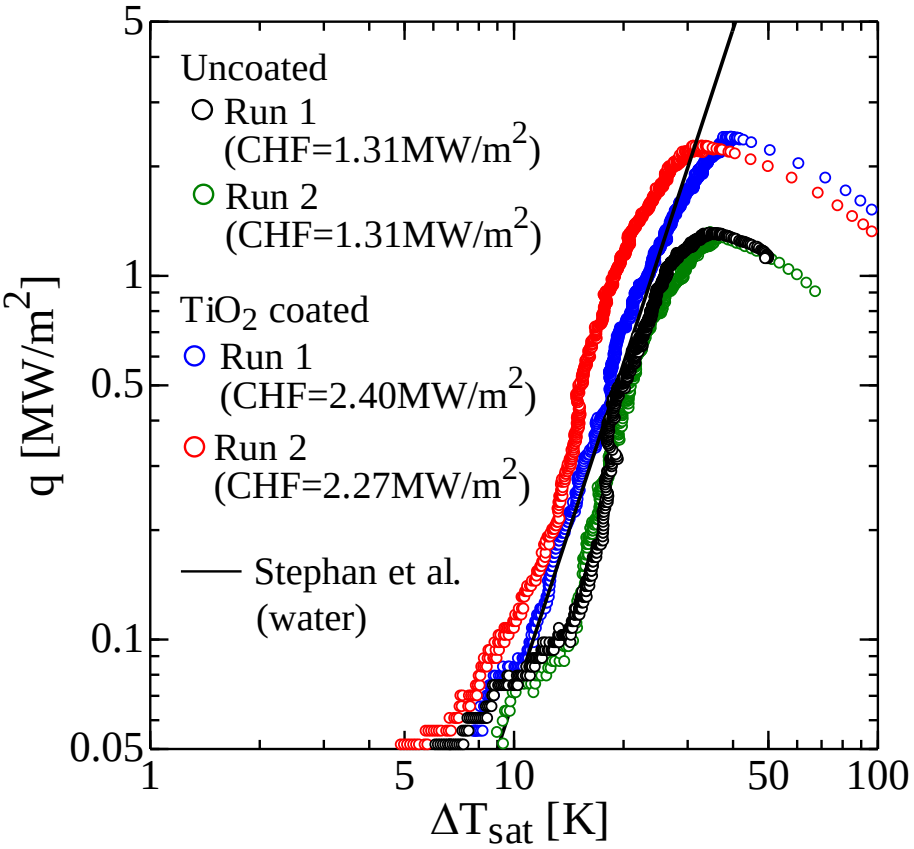

Fig.6 Boiling curves for uncoated and TiO_2 coated surfaces

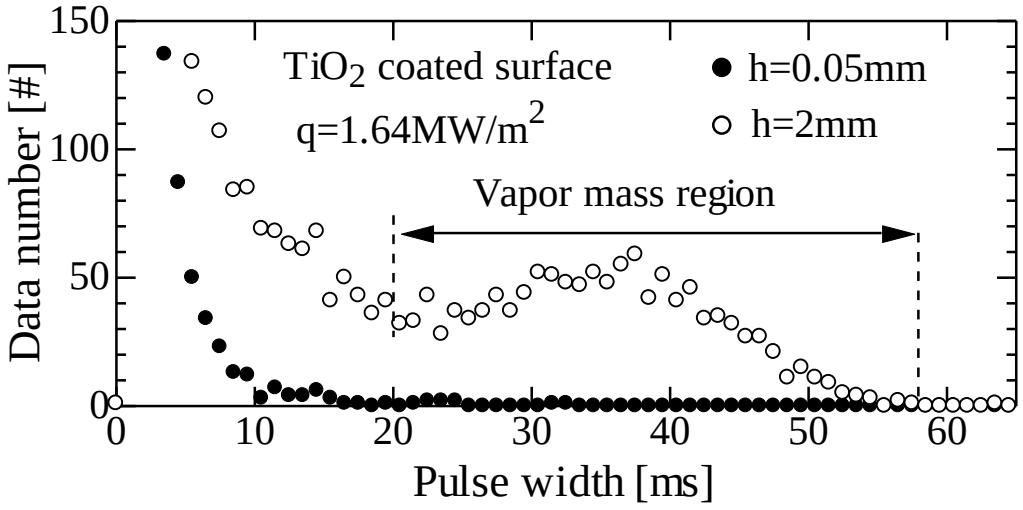

Fig.7 Pulse width spectrums above the heating surface at h=0.05 mm and h=2 mm

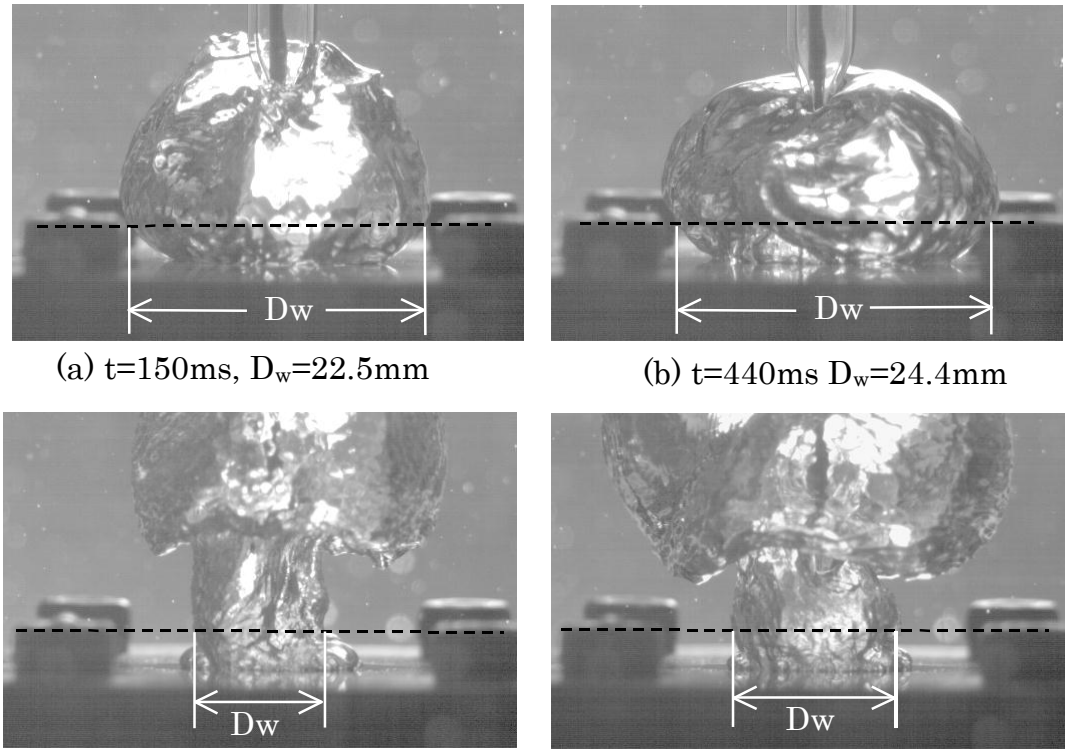

(a) t=150ms, D_w=22.5mm (b) t=440ms D_w=24.4mm

(c) t=117ms. D_w=8.7mm (d) t=186ms. D_w=9.8mm

Fig.8 Boiling appearance (TiO_2 coated surface, q=1.96MW/m^2)

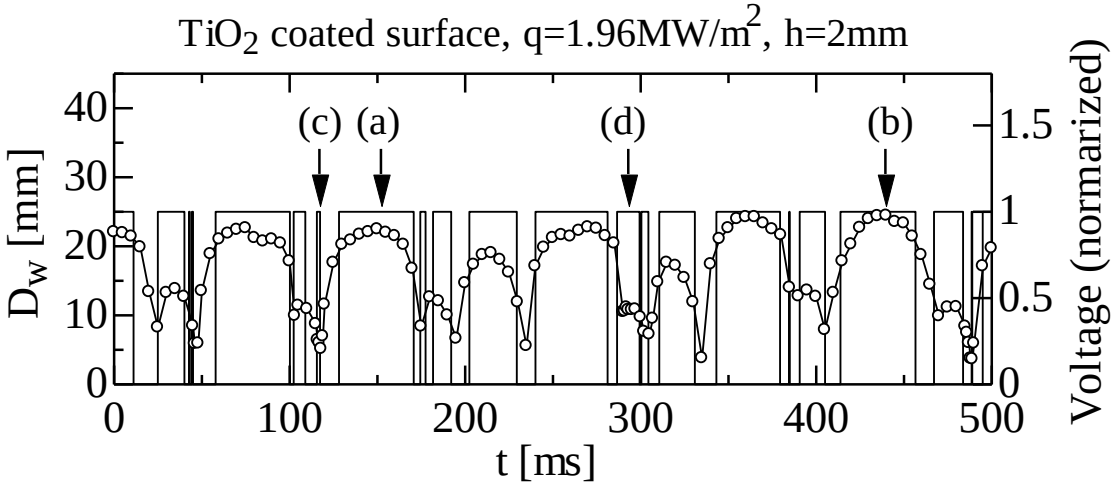

Fig.9 Width of coalesced bubbles and binary probe signals measured at 2mm above the heating surface

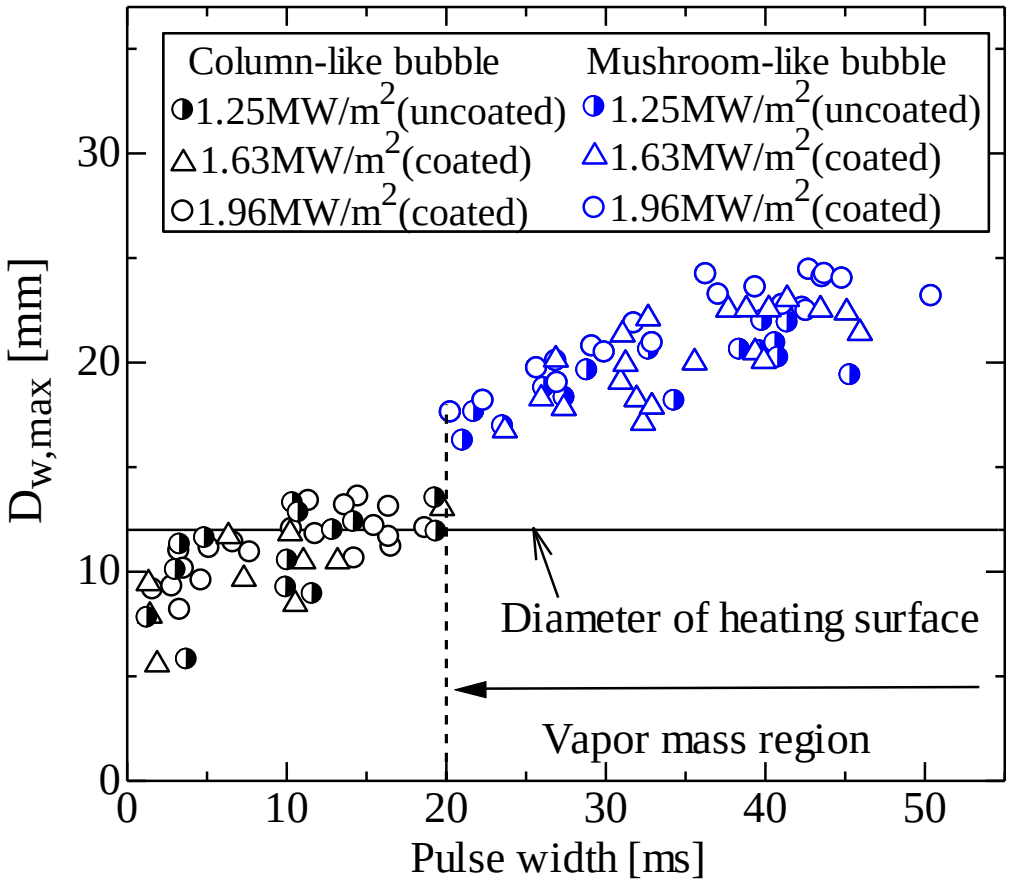

Fig.10 Plot of maximum width of coalesced bubbles and pulse widths

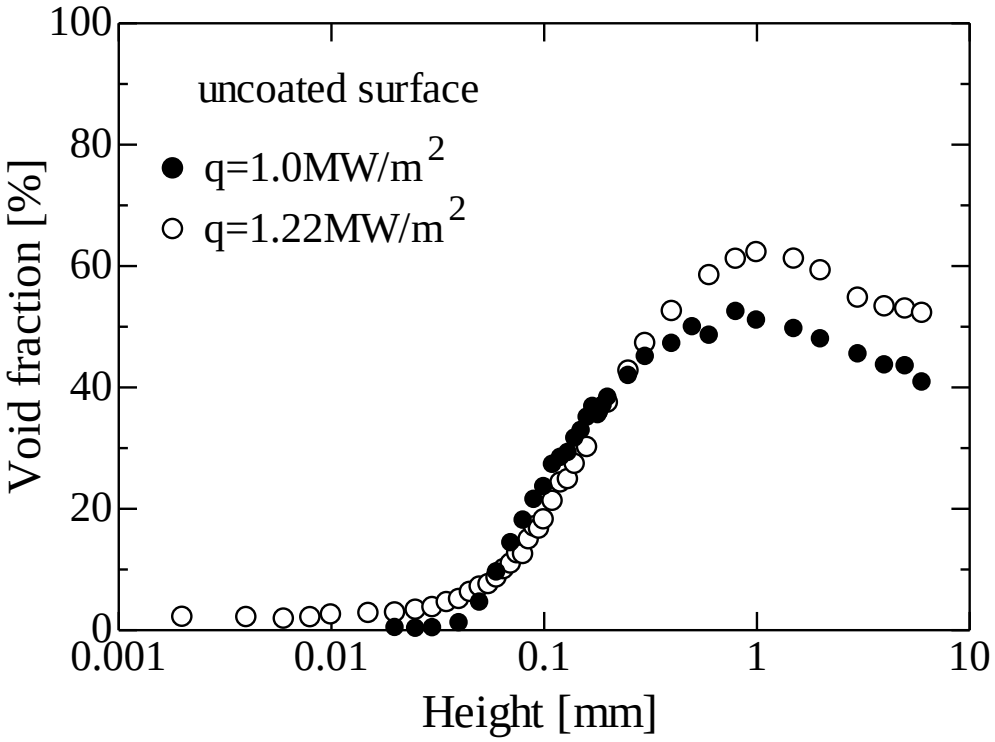

Fig.11 Void fraction distributions (uncoated surface)

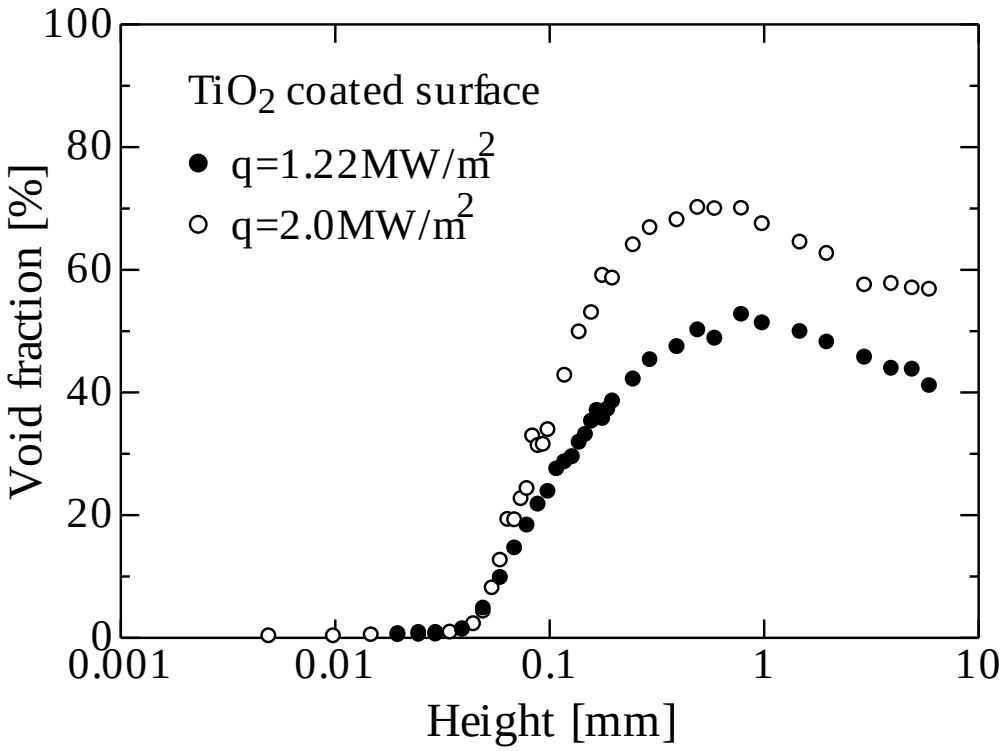

Fig.12 Void fraction distributions (TiO_2 coated surface)

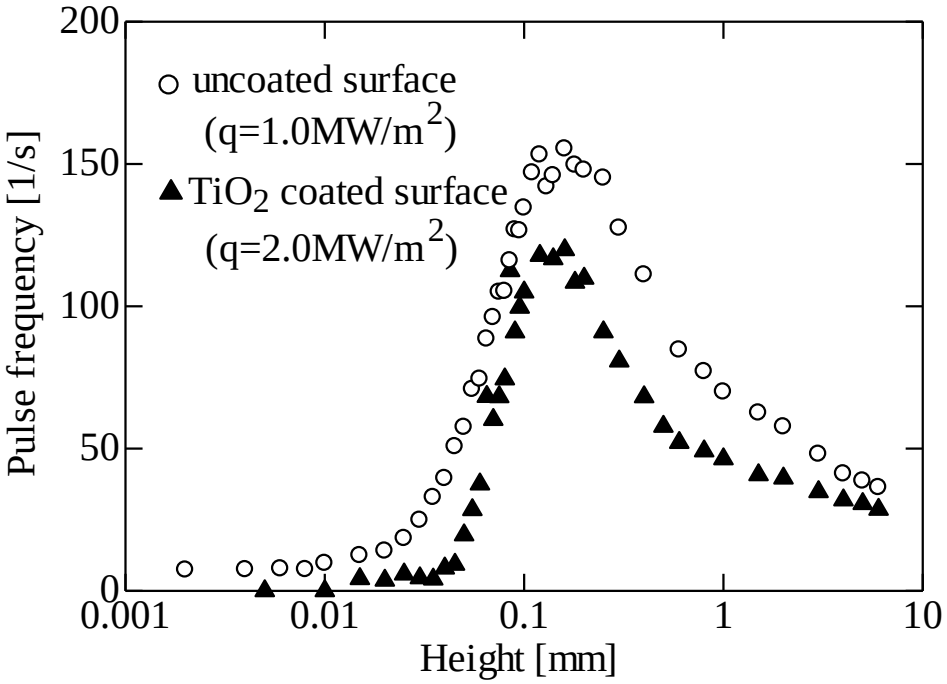

Fig.13 Pulse frequency distributions

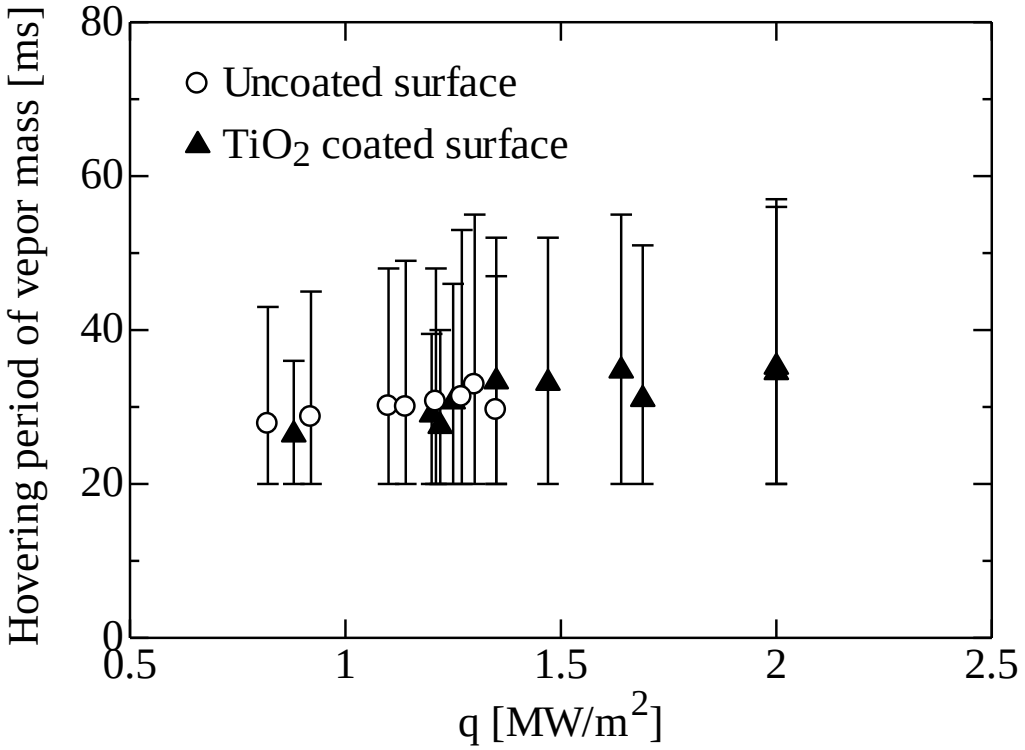

Fig.14 Hovering periods of vapor masses for uncoated and TiO_2 coated surfaces

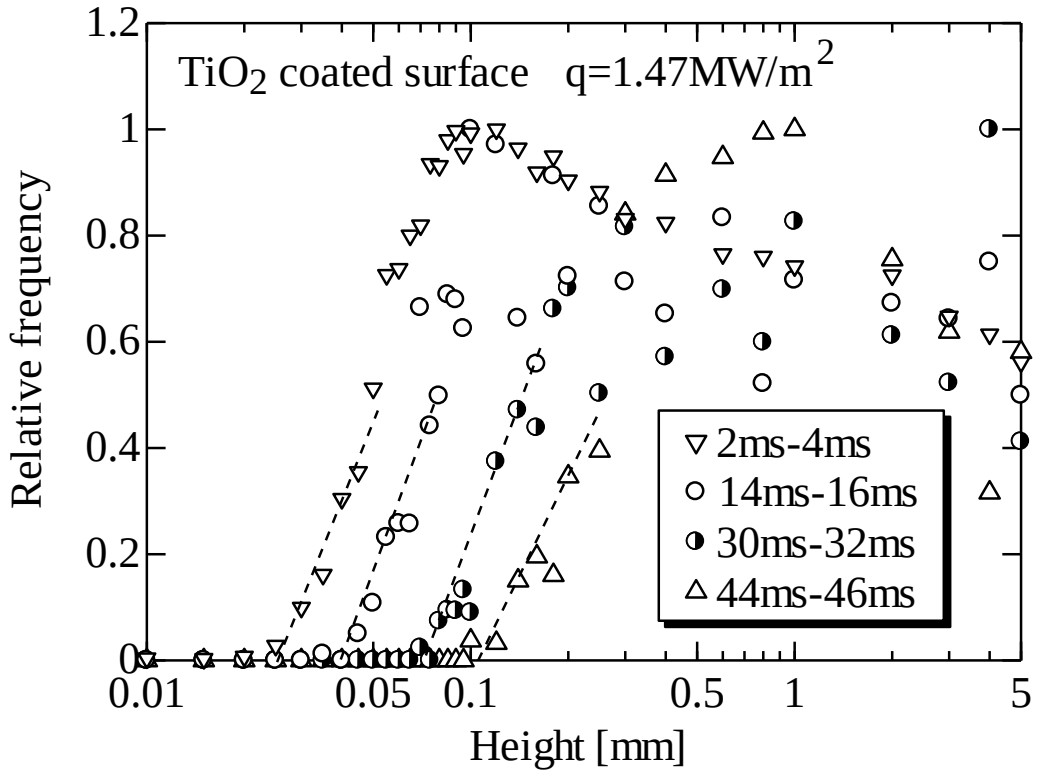

Fig.15 Frequency distributions for the 2-4, 14-16, 30-32 and 36-38 ms-wide pulses

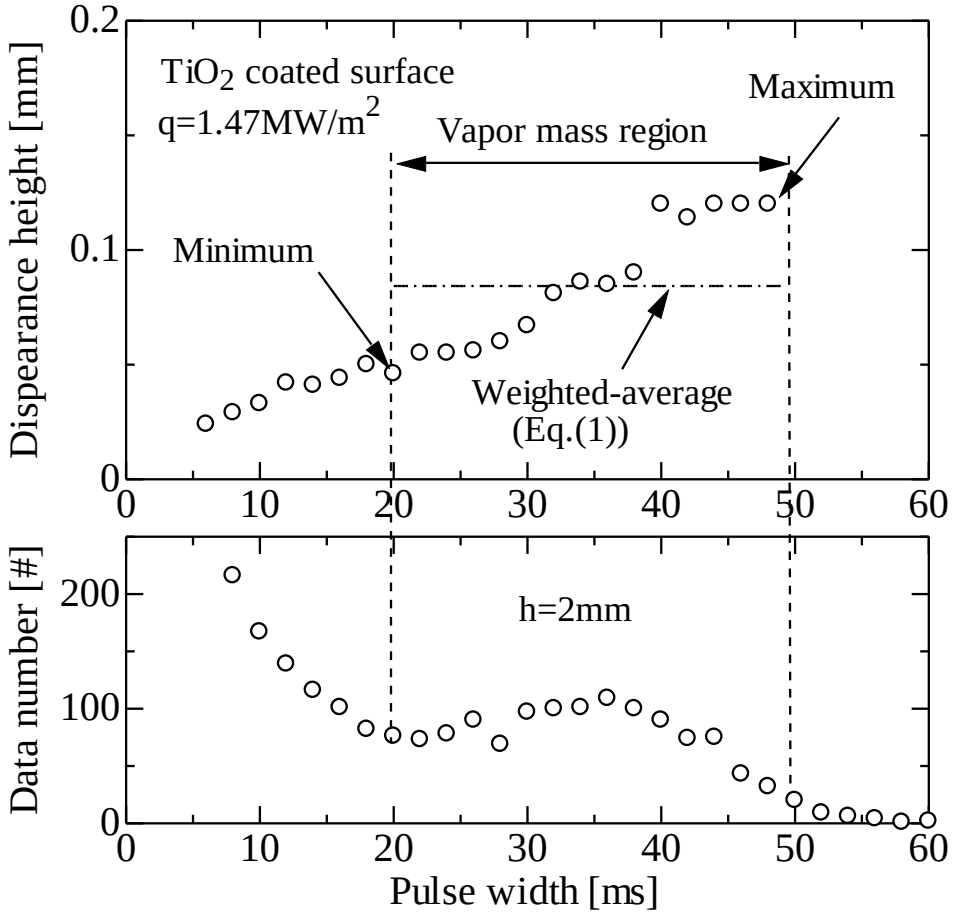

Fig.16 Distance from heating surface where pulses disappear and incidence of pulses at h=2 mm

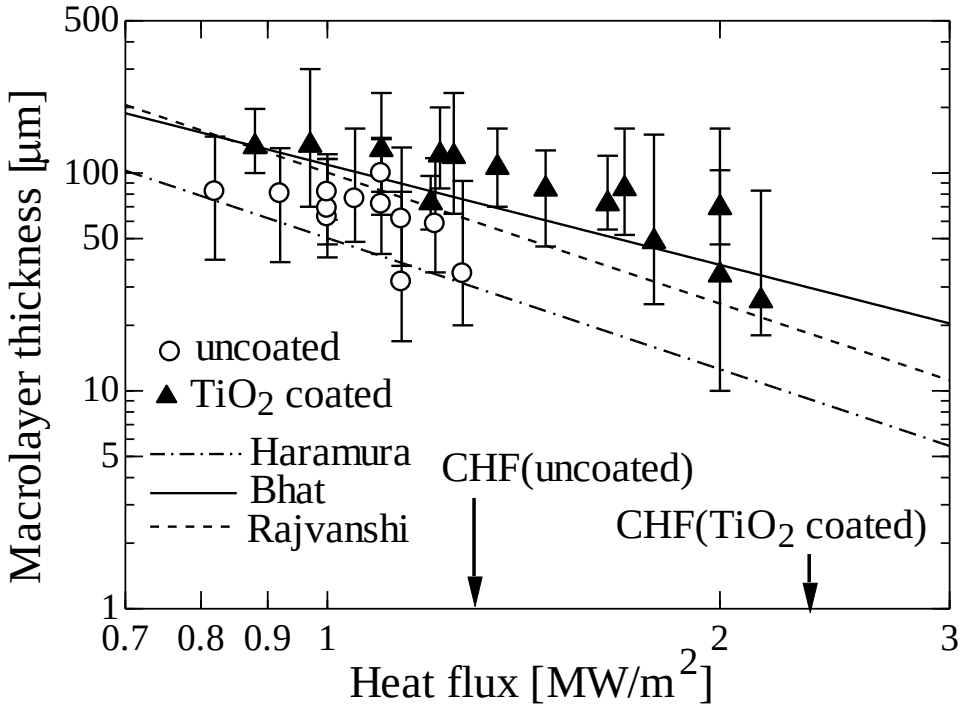

Fig.17 Macrolayer thickness for uncoated and TiO_2 coated surfaces

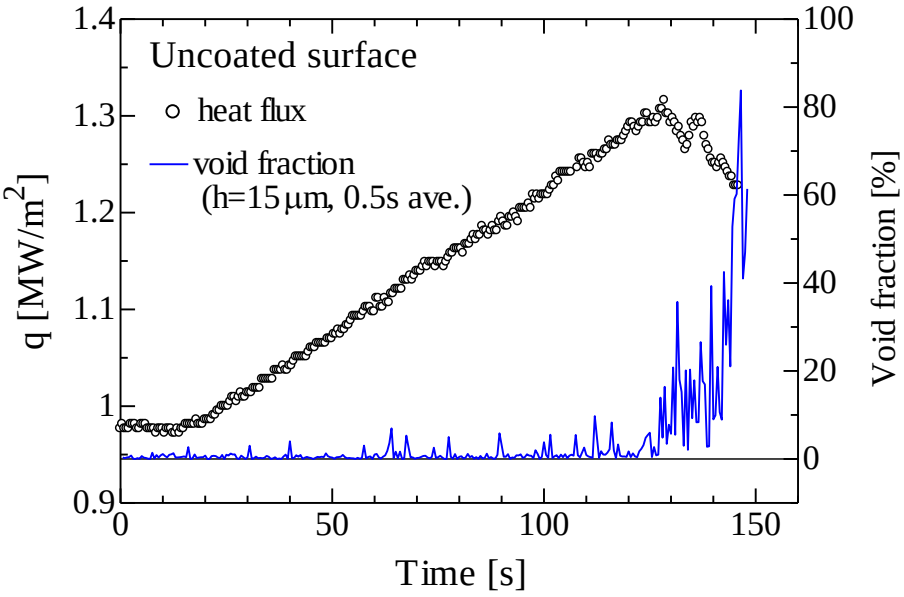

(a) Uncoated surface

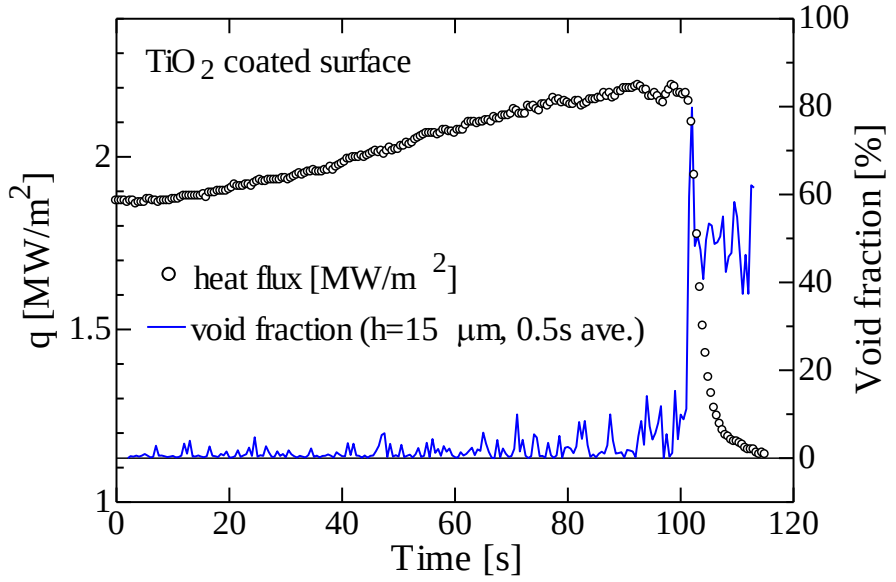

(b) TiO_2 coated surface

Fig.18 Change in heat fluxes and void fractions at h=15 μm before and after CHF

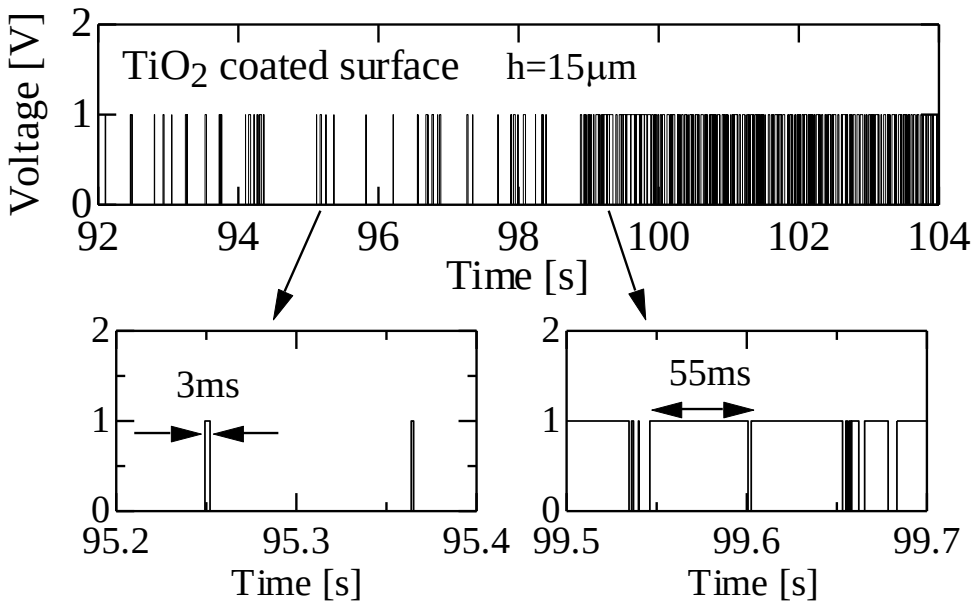

Fig.19 Digitized probe signals before (left) and after (right) CHF